Letters in Applied NanoBioScience
Open-Access Journal (ISSN: 2284-6808)

Article
Volume 13, Issue 3, 2024, 105
https://doi.org/10.33263/LIANBS133.105

Bio-Sensing of [S & N]–Heterocyclic Carbene Corrosion Inhibitors by Sn–Embellished on the Al-Mg Crystal Surface: A DFT Study

Fatemeh Mollaamin [1,*], Farnoush Naghsh [2], Neda Samiei Soofi [2], Karim Zare [2]

[1] Department of Biomedical Engineering, Faculty of Engineering and Architecture, Kastamonu University, Kastamonu, Turkey
[2] Department of Chemistry, Science and Research Branch, Islamic Azad University, Tehran, Iran
* Correspondence: fmollaamin@kastamou.edu.tr ; smollaamin@gmail.com (F.M.);

Scopus Author ID 35848813100
Received: 23.05.2023; Accepted: 11.08.2023; Published: 25.07.2024

Abstract: The partial electron density states (PDOS) have described an obvious charge accumulation between the Al–Mg alloy and the doped atom of Sn through the recognition of the conduction band region. The physicochemical properties of adsorption on the nanosurface are one of the fundamental parameters for determining and choosing the Langmuir adsorption through IR, NMR, UV-VIS, and HOMO/LUMO and charge distribution results. Therefore, in this article, the ONIOM approach has been performed with a three-layered level of the high level of DFT method using EPR-III, 6-31+G (d,p) and LANL2DZ basis sets by the physicochemical software of Gaussian 16 revision C.01, a medium semi-active part that includes important electronic contributions, and a low-level part that has been handled using MM2 force field approaches. Comparing to ΔG^{o}_{ads} amounts approved a good agreement among computed results, as well as the correctness of the selected isotherm for the adsorption process of benzotriazole → Al-Mg-Sn, 2-mercaptobenzothiazole→ Al-Mg-Sn, 8- hydroxyquinoline → Al-Mg-Sn, and 3-amino-1, 2, 4-triazole-5-thiol → Al-Mg-Sn. The infrared spectra for each of these inhibitor-metal alloy surface have been introduced in the frequency range around 500cm^{-1}-4500cm^{-1} for benzotriazole → Al-Mg-Sn, 2-mercaptobenzothiazole → Al-Mg-Sn, 8- hydroxyquinoline → Al-Mg-Sn and 3-amino-1, 2, 4-triazole-5-thiol → Al-Mg-Sn with the sharpest peak approximately around 1750cm^{-1} for benzotriazole → Al-Mg-Sn, 2000cm^{-1} for 2-mercaptobenzothiazole → Al-Mg-Sn, 3000cm^{-1} for 8- hydroxyquinoline → Al-Mg-Sn and 3900cm^{-1} for 3-amino-1, 2, 4-triazole-5-thiol → Al-Mg-Sn. Nuclear magnetic resonance has certainly focused on aluminum shielding in the intra-atomic interaction with aluminum, magnesium, and silicon and simultaneously interatomic interaction with other atoms in organic inhibitors through a variety of high, medium, and low layers of ONIOM methods. Al-Sn(14), Al-Sn(19), and Al-Sn(21) in the Al-Mg-Sn alloy surface with the highest fluctuation in the shielding tensors of NMR spectrum generated by intra-atomic interaction direct us to the most influence in the neighbor atoms generated by interatomic reactions of N→Al, O→ Al, S→ Al through the coating and adsorbing process of Langmuir adsorption. Moreover, based on the computed amounts of UV-VIS spectra for benzotriazole, mercaptobenzothiazole, 8-hydroxyquinoline and 3-amino-1, 2, 4-triazole-5-thiol adsorbed on the Al-Mg-Sn alloy surface, there are maximum adsorption bands between 500nm-2000nm wavelengths for these organic heterocyclic inhibitors joint metal alloy which has illustrated a certain peak with approximately 1000nm wavelength.

Keywords: Sn-doped Al-Mg alloy; langmuir adsorption; benzotriazole; 2-mercaptobenzothiazole; 8-hydroxyquinoline; 3-amino-1, 2, 4-triazole-5-thiol;DFT.

1. Introduction

Aluminum alloys are formed by the special alloying elements Cu, Mg, Mn, Si, Sn, Ni, and Zn. The lightweight or corrosion resistance of aluminum alloys makes them suitable for use in engineering structures and components [1-8].

Aluminum-silicon (Al-Si) is one of the most important aluminum alloys with high amounts of silicon in casting and has a large limitation of usages in the aerospace and automotive industries through the best combination of mechanical properties, as well as good wear resistivity and corrosion resistance [9-11].

Si element in Al-Si-based cast alloys impacts tensile properties at both room and high temperatures, but its role becomes more important in the lack of alloy elements such as Mg, Fe, and Cu [12-18].

Some elements like Cu and Mg added to Al alloys ameliorate the mechanical attributes and conduct the alloy to reply to the heat sealing. The existence of magnesium also increases resistance and reduces the rate of strength loss at high temperatures in the alloys. Aluminum-magnesium (Al-Mg) alloys are lighter than other aluminum alloys and much less flammable than other alloys of high amounts of magnesium. The magnificent enhancement in resistance at elevated temperatures was accomplished after solution treatment through activating settlement, becoming hard through Mg possessing phases [19,20].

Among the various methods that minimize the corrosion of metal surfaces, its inhibition by organic molecules is one of the most applicable methods because of its stability and low cost [21-25]. A lot of research has been dedicated to the application of efficient heterocyclic and heteroatomic processes, including organic compounds that facilitate the anticorrosion attributes of metal surfaces and alloys. The existence of heteroatoms containing O, S, N, and P atoms, aromatic rings, and multiple bonds with π-electrons in these inhibitors help extensively to the formation of inactive blocks on metal surfaces and alloys, so closing the active sites of corrosion [26-30].

Aluminum-gallium (Al-Ga), which is a degenerate alloy, is obtained from liquid gallium diffusing the crystal structure of Ga metal. This alloy is so fragile that it is broken under a little pressure. Al-Ga alloy is also chemically more fragile because it prevents Al from forming a protective oxide layer. This element and its alloys are usually employed as experimental fluids for modeling liquid and solid dynamics in planetary cores. Al-Ga can react with H_2O molecules to produce Al oxide, Ga metal, and hydrogen gas. Al reacts in air to generate an inactive aluminum oxide layer and doesn't react with water. Aluminum-gallium alloy can form Al nanoparticles for the hydrogen-creating reaction [31-33].

Based on some research, benzotriazole, 2-mercaptobenzothiazole, 8-hydroxyquinoline, and 3-amino-1, 2, 4-triazole-5-thiol are organic cyclic inhibitors for metal, semi-metals, or non-metals surfaces and their alloys by preventing undesirable surface reactions. It is obvious that a passive layer, containing a complex between the surface and these inhibitors, is generated when the surface is immersed in a solution consisting of benzotriazole, 2-mercaptobenzothiazole, 8-hydroxyquinoline, and 3-amino-1, 2, 4-triazole-5-thiol. The passive layer is insoluble in aqueous and many organic solutions. There is a positive connection between the thickness of the passive layer and the efficiency of preventing corrosion [34-37].

In the present work, we have investigated adding some alloying elements of magnesium and silicon to the aluminum surface forming Al-Mg-Sn complex, which has been coated with

organic compounds of benzotriazole, 2-mercaptobenzothiazole, 8- hydroxyquinoline, and 3-amino-1, 2, 4-triazole-5-thiol as the corrosion inhibitors of Al-Mg-Sn alloy surface.

2. Materials and Methods

2.1. Organic corrosion inhibitors.

Recently, some researchers have investigated the possibility of organic compounds being employed as corrosion inhibitors for Al and its alloys because they consist of several heteroatoms (N, S, O, and P) that act as active adsorption centers. In this verdict, we discuss the use of organic compounds of benzotriazole, 2-mercaptobenzothiazole, 8-hydroxyquinoline, and 3-amino-1, 2, 4-triazole-5-thiol as the corrosion inhibitors of Al-Mg-Sn alloy surface [38-40].

In this research, it has been attributed the inhibiting effect of the benzotriazole, 2-mercaptobenzothiazole, 8- hydroxyquinoline, and 3-amino-1, 2, 4-triazole-5-thiol on the adsorption of a stable complex formed on the aluminum alloy of Al-Mg-Sn surface.

2.2. Langmuir adsorption theory.

The study involving the influence of the organic inhibitors in solution and the nature of the corrosive aluminum alloys on the adsorption bond strength yields information about the mechanism of interaction of the inhibitor with the Al alloys surface, which, in turn, Langmuir adsorption isotherms provide excellent. The Langmuir isotherm is widely used to identify inhibitor adsorption status specification [41,42].

The adsorption of benzotriazole, 2-mercaptobenzothiazole, 8-hydroxyquinoline, and 3-amino-1, 2, 4-triazole-5-thiol as corrosion inhibitors on the aluminum alloy surface of Al-Mg-Sn in NaCl solution were assigned by the most suitable Langmuir isotherm, which exhibits the chemisorptive nature of the bond between the inhibitor molecules and the Al-Mg-Sn alloy surface, the equilibrium distribution of ions of the adsorbing compound between the solid and liquid phases, and a monolayer attribute.

The adsorbed molecules are kept on the Al-Mg-Sn alloy surface with chemisorbed inhibitors having high protection (Scheme 1).

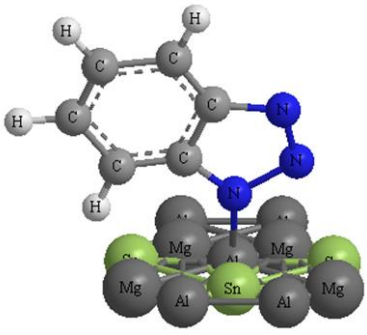

(a)

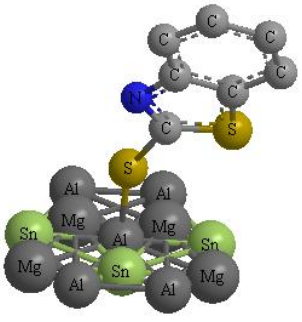

(b)

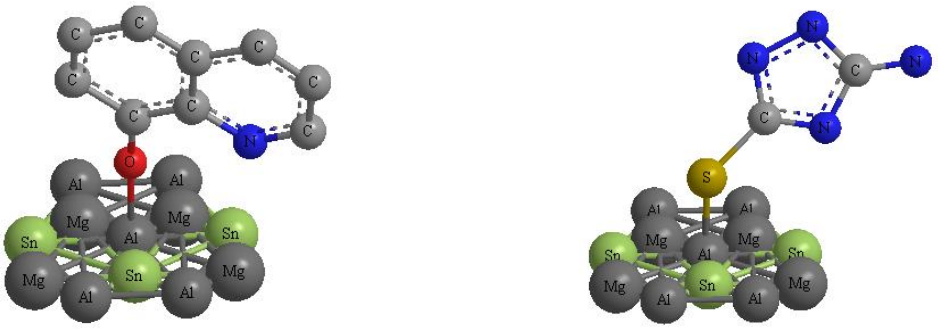

(c) **(d)**

Scheme 1. Langmuir adsorption of the organic corrosion inhibitors of **a)** benzotriazole; **b)** 2-mercaptobenzothiazole; **c)** 8- hydroxyquinoline; **d)** 3-amino-1, 2, 4-triazole-5-thiol onto Al-Mg-Sn alloy surface.

2.3. ONIOM method.

In this work, the advanced ONIOM simulation was performed. So, the combination of three levels in decreasing order of accuracy, including high, medium, and low levels of theory, has been defined. High-level has been done using the DFT method of Cam-B3LYP with 6-31+G (d,p) basis set for some hydrogen, carbon, oxygen, and sulfur atoms in the inhibitor; some oxygen and sulfur atoms in the adsorption site; EPR-III basis set for nitrogen atoms in the inhibitor and adsorption site; LANL2DZ for some aluminum, magnesium and tin atoms in the adsorption sites. Medium-level research has been done on the other hydrogen, carbon, nitrogen, oxygen, and sulfur atoms in the adsorption site using semi-empirical methods. Finally, a low-level has been performed on the other aluminum, magnesium, and tin atoms with MM2 force fields (Scheme 2) [43-47]: $E_{ONIOM} = E_{High} + E_{Medium} + E_{Low}$ **(1)**

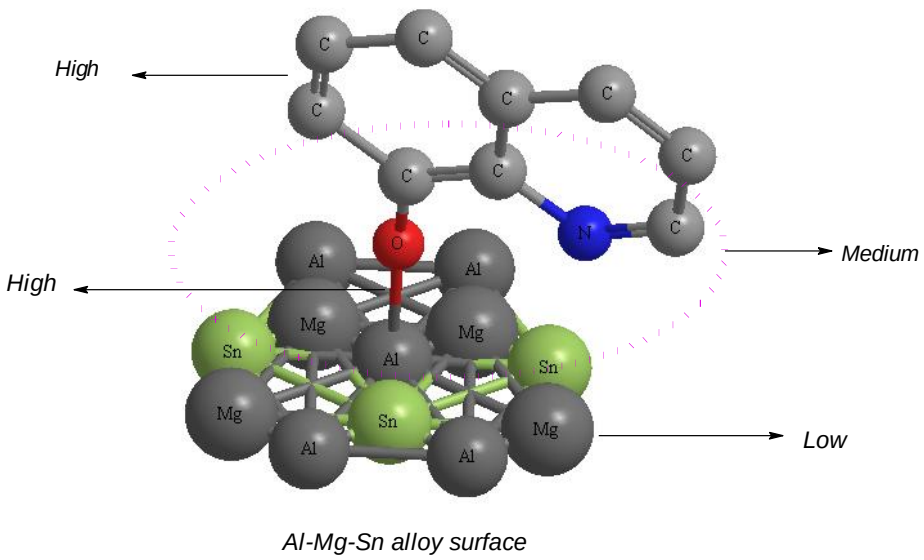

Scheme 2. The ONIOM layer of adsorption mechanism for 3-amino-1, 2, 4-triazole-5-thiol as a corrosion inhibitor onto Al-Mg-Sn alloy surface based on optimized coordination.

On the other hand, the three-layered method of ONIOM lets us discover a larger system that is more exactly than the one-layered model, which could behave as a medium-sized system precisely like a ground system with acceptable accuracy [48-54].

Therefore, this three-layered pattern has been applied for effective barriers of benzotriazole, 2-mercaptobenzothiazole, 8-hydroxyquinoline, and 3-amino-1, 2, 4-triazole-5-thiol adsorbing onto Al-Mg-Sn alloy surface (Scheme 2).

We have calculated the structures using the density functional theory (DFT) on the mechanisms onto Al-Mg-Sn alloy surfaces up to adsorbed in the active sites of organic inhibitors by nitrogen, oxygen, and sulfur atoms of benzotriazole, 8- hydroxyquinoline, 2-mercaptobenzothiazole, and 3-amino-1, 2, 4-triazole-5-thiol, respectively.

We have found that the surface binding site preferences of N-atom of benzotriazole, O-atom of 8- hydroxyquinoline and S-atom of both 2-mercaptobenzothiazole and 3-amino-1, 2, 4-triazole-5-thiol in adsorption site is largely affected by the presence of neighboring atoms. The calculated N→Al, O→Al, and S→Al pair distribution functions have indicated that the formation of clusters directs to shorter N→Al, O→Al, and S→Al bond lengths when compared to the homogeneous growth (Scheme2).

In this work, the atomic structure of the Al-Mg-Sn alloy surface has been built using GaussView 6.06.16 [55] and calculated by the Gaussian 16 program package [56] through geometry coordination. Result observations have represented that the Al-Mg-Sn alloy surface calculated with the achieved structure parameters is in good agreement with those metal alloys attained from other experimental calculations [57-62].

2.4. DFT calculations.

Hybrid functional is a group of approximations for the exchange-correlation energy functional in DFT (Density Functional Theory), which combines a part of exact exchange from HF (Hartree–Fock theory) method with the rest of the exchange-correlation energy from other information such as empirical or ab initio methodologies. Therefore, the exact exchange energy function is illustrated by the Kohn–Sham orbitals instead of the density, so it is placed as the indirect density function. This study has applied the influence of the hybrid functional of a three-parameter basis set of B3LYP (Becke, Lee, Yang, Parr) within the framework of DFT upon theoretical calculations [63]. The popular B3LYP (Becke, three-parameter, Lee–Yang–Parr) exchange-correlation functional is [63].

The Al-Mg-Sn alloy surface was built using a rigid system and Z-Matrix format, in which a blank line was placed. After that, the following information has been illustrated. The rigid PES has been performed at CAM-B3LYP functional, and employing 6-31+ G (d,p) /EPRIII /LANL2DZ basis sets to assign HOMO, LUMO, Mulliken charges, nuclear magnetic resonance properties, dipole moment, thermodynamic characteristics and other quantum properties for this study for benzotriazole, 8- hydroxyquinoline, 2-mercaptobenzothiazole, and 3-amino-1, 2, 4-triazole-5-thiol adsorbing onto the Al-Mg-Sn alloy surface using Gaussian 16 program package [56]. The input files for the organic corrosion inhibitors adsorbed onto the Al-Mg-Sn surface have been provided with GaussView 6.06.16 [55]. For the Al-alloy surface, the small energy difference between the formations of inhibitor → Al-Mg-Sn alloy complex can direct us to a pretty coated surface for preventing corrosion.

3. Results and Discussion

In this article, the susceptibility of organic inhibitors (benzotriazole, 2-mercaptobenzothiazole, 8- hydroxyquinoline, and 3-amino-1, 2, 4-triazole-5-thiol),

characteristics of aluminum alloy surface (Al-Mg-Sn) and adsorption conditions are considerable.

3.1. Electronic properties of surface.

The electronic structures of Al–Al, Al–Mg, and Al–Mg–Sn surfaces have been analyzed to simplify subsequent discussion for interfacial electronic properties through the projection of particular orbital of particular atom on the density of states (PDOS) by using density functional theory (DFT) and LANL2DZ basis set. The PDOS has described the orbital states of pristine Al-Al surface, binary Al–Mg alloy, and the rate of dominancy of Sn-doped on the Al–Mg alloy by forming ternary Al–Mg–Sn surface through the conduction band (Figure 1).

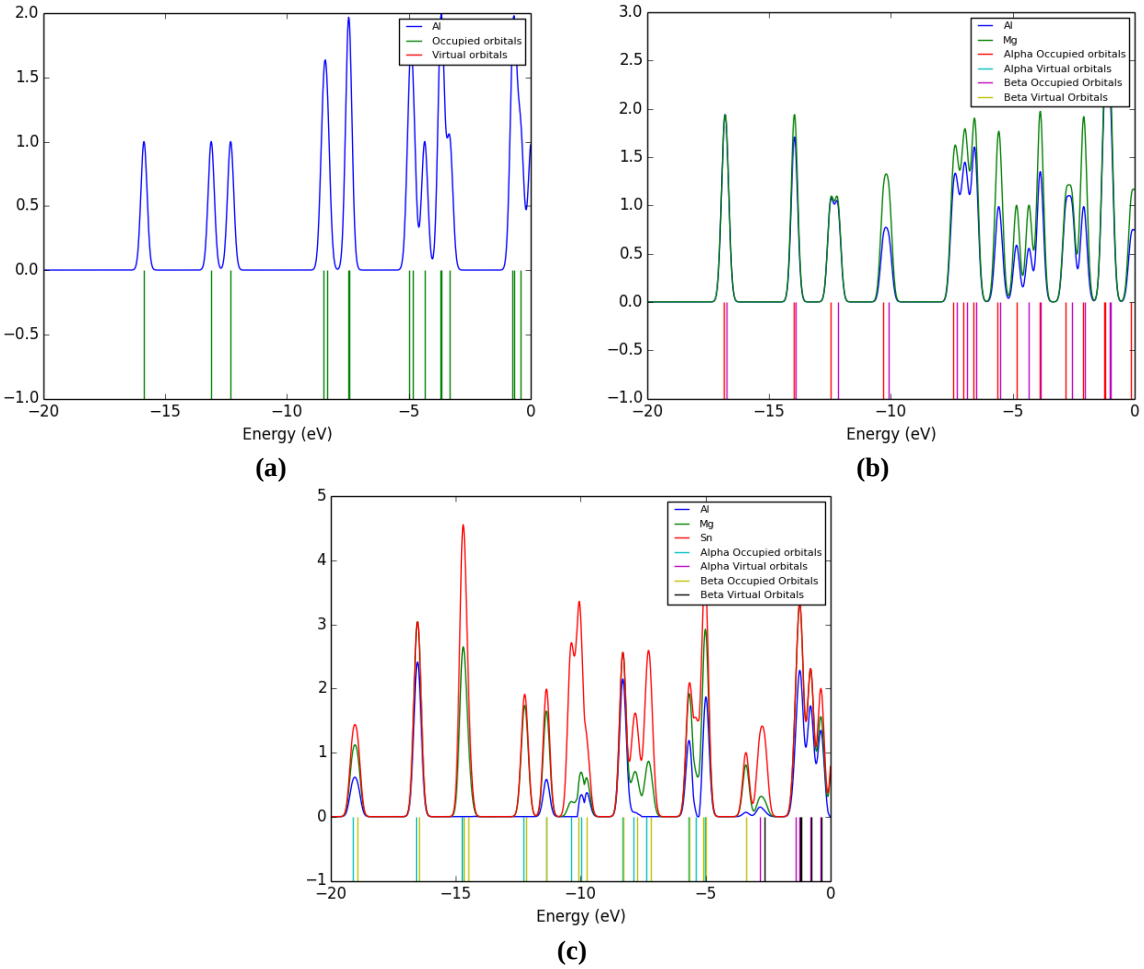

Figure 1. PDOS of **a)** Al–Al; **b)** Al–Mg; **c)** Al–Mg–Sn nanoalloys with Fermi level =0.

A distinct metallic feature can be observed in the Al–Mg–Sn alloy because of the strong interaction between the *p* states of Al and the *d* states of Sn close to the Fermi energy. In addition, the presence of covalent features for this alloy has exhibited the identical energy amount and figure of the PDOS for the *p* orbitals of Al and *d* orbitals of Sn.

Figure 1(a) shows that the Al states in the Al–Al alloy have more contribution at the middle of the conduction band between –5 to –15eV. Al and Mg states in the Al–Mg alloy have similar contributions at the middle of the conduction band between –5 to –15eV, while the contribution of Al states is weaker than Mg states (Figure 1b). But, Sn states in the Al–Mg–Sn alloy reveal the expanded contribution with the conduction band between –1 to –20eV, as Sn states are stronger than the Mg state and Al states (Figure 1c).

The results are also approved by the partial electron density (PDOS), which has shown a certain charge association between the Al–Mg alloy and the doped Sn element. In other words, the Sn states have large contributions in the valence band, while Mg states and Al states have acceptable contributions but represent weaker states than Mg states and Al states. Thus, the above results exhibit that the cluster dominant of metallic feature and a certain degree of covalent trait can illustrate the increase in the conducting direct band gap of Sn-doped on the Al–Mg alloy.

3.2. Infrared spectroscopy analysis.

Based on binary systems in thermodynamic analysis, the liquid phase was illustrated by applying the accompanying solution model, with aluminum, magnesium, tin, and Mg_2Sn as the species. Moreover, a single ternary interaction parameter was discovered to be adequate to match all the experimental information. Aluminum (fcc) and magnesium (cph) were explained as disordered substitutional solutions. In addition, the allotropic forms of tin and the binary structures of Mg_2Sn, Mg_2Al_3 (β), and ε phases were considered stoichiometric phases [64-67].

The IR spectrum for each of these compounds has been seen in the frequency range around 500cm^{-1}-4500cm^{-1} for benzotriazole → Al-Mg-Sn, 2-mercaptobenzothiazole → Al-Mg-Sn, 8- hydroxyquinoline → Al-Mg-Sn and 3-amino-1, 2, 4-triazole-5-thiol → Al-Mg-Sn with the sharpest peak approximately around 1750cm^{-1} for benzotriazole → Al-Mg-Sn, 2000cm^{-1} for 2-mercaptobenzothiazole → Al-Mg-Sn, 3000cm^{-1} for 8- hydroxyquinoline → Al-Mg-Sn and 3900cm^{-1} for 3-amino-1, 2, 4-triazole-5-thiol → Al-Mg-Sn (Figure 2a-d).

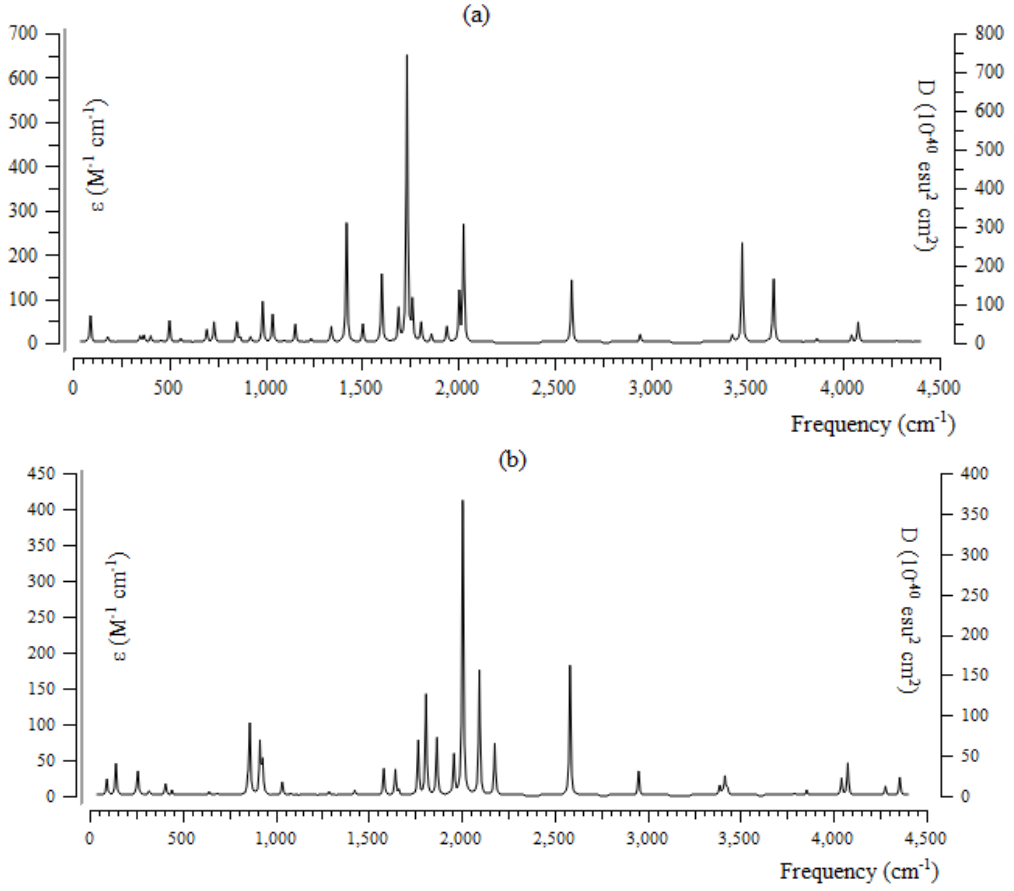

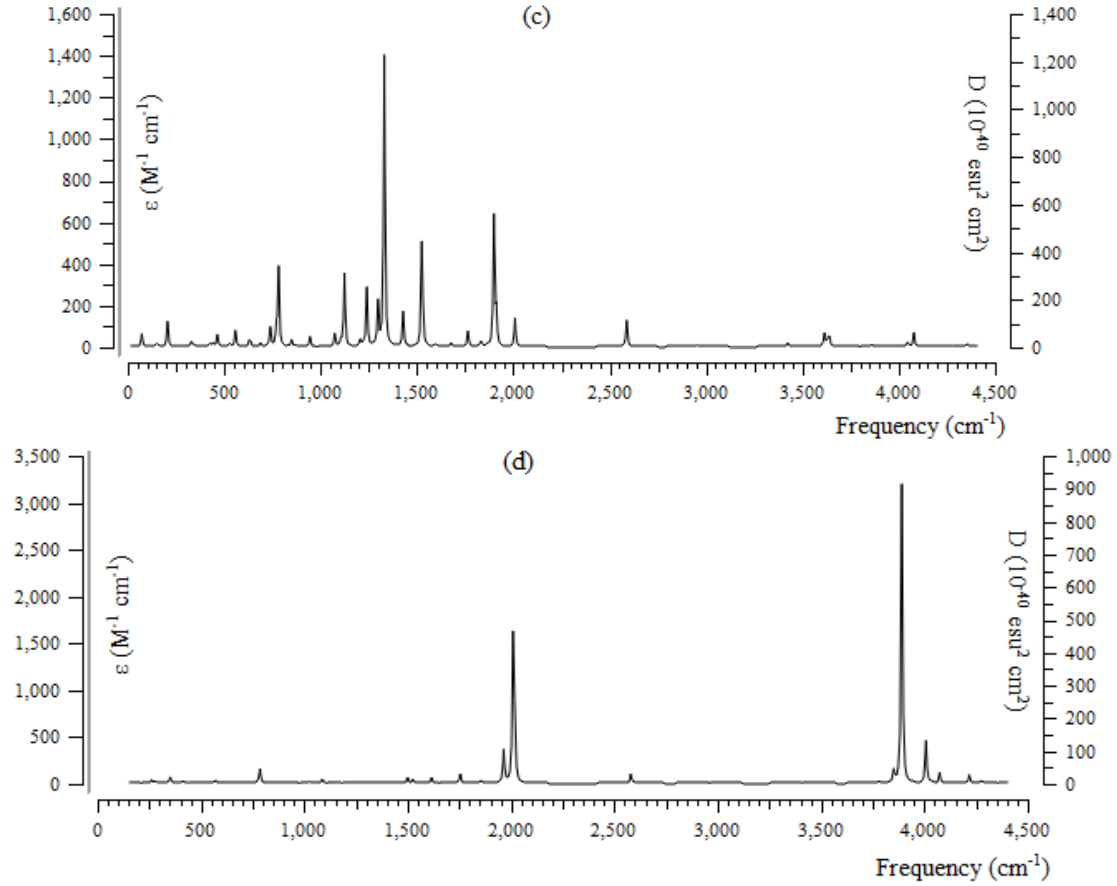

Figure 2. Changes of frequency (cm^{-1}) through the IR spectra for **a)** benzotriazole → Al-Mg-Sn; **b)** 2-mercaptobenzothiazole→ Al-Mg-Sn; **c)** 8- hydroxyquinoline → Al-Mg-Sn; **d)** 3-amino-1, 2, 4-triazole-5-thiol → Al-Mg-Sn using CAM-B3LYP method with 6-31+ G (d,p) /EPRIII /LANL2DZ basis sets.

The infrared (IR) calculations have been accomplished for an aluminum alloy of Al-Mg-Sn interacting with four organic inhibitors including benzotriazole, 2-mercaptobenzothiazole, 8- hydroxyquinoline, and 3-amino-1, 2, 4-triazole-5-thiol adsorbed onto this alloy surface which produce the complexes of benzotriazole → Al-Mg-Sn, 2-mercaptobenzothiazole→ Al-Mg-Sn, 8- hydroxyquinoline → Al-Mg-Sn, and 3-amino-1, 2, 4-triazole-5-thiol → Al-Mg-Sn at CAM-B3LYP level of theory employing 6-31+ G (d,p) /EPRIII /LANL2DZ basis sets to obtain the more accurate equilibrium geometrical parameters, physical and thermodynamic properties for each of the determined structure (Table 1).

Table 1. The Physico-chemical properties of adsorption for benzotriazole, 2-mercaptobenzothiazole, 8-hydroxyquinoline, and 3-amino-1, 2, 4-triazole-5-thiol as corrosion inhibitors on the aluminum alloy surface of Al-Mg-Sn in NaCl solution at 300K.

Compound	$\Delta H^o \times 10^{-5}$ (kcal/mol)	$\Delta G^o \times 10^{-5}$ (kcal/mol)	S^o (cal/K.mol)	Dipole moment (Debye)
Al-Mg-Sn	-124.6274	-124.6276	79.866	2.2570
Benzotriazole	-24.5172	-24.5196	80.255	3.3166
Benzotriazole → Al-Mg-Sn	-127.0736	-127.0739	95.509	5.4914
2-mercaptobenzothiazole	-69.5234	-69.5260	85.643	2.5108
2-mercaptobenzothiazole→Al-Mg-Sn	-131.5725	-131.5728	98.135	4.4890
8- hydroxyquinoline	-29.5526	-29.5551	83.336	1.6389
8- hydroxyquinoline →Al-Mg-Sn	-127.5784	-127.5787	99.118	2.2719
3-amino-1, 2, 4-triazole-5-thiol	-43.1336	-43.1358	73.839	1.5672
3-amino-1, 2, 4-triazole-5-thiol →Al-Mg-Sn	-128.9338	-128.9340	89.460	3.1408

From Figure 3, it could be found that the maximum of the Langmuir adsorption isotherm plots based on ΔG^{o}_{ads} may depend on the interactions between the inhibitor structures and the Al-alloy surfaces. In fact, in comparison to ΔG^{o}_{ads} amounts confirmed a good agreement among calculated results, as well as the correctness of the selected isotherm for the adsorption process of benzotriazole → Al-Mg-Sn, 2-mercaptobenzothiazole→ Al-Mg-Sn, 8-hydroxyquinoline → Al-Mg-Sn, and 3-amino-1, 2, 4-triazole-5-thiol → Al-Mg-Sn (Figure 3).

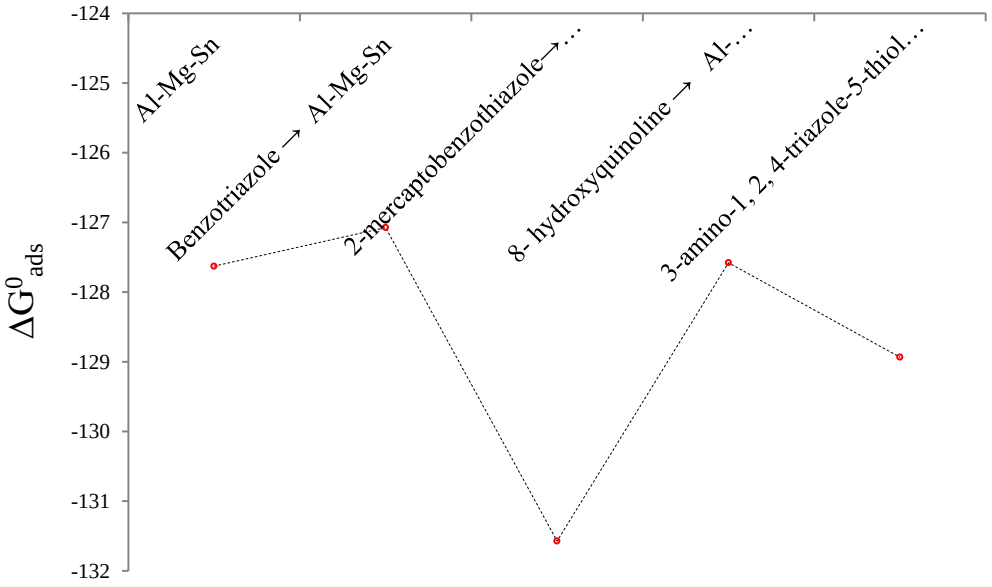

Figure 3. The changes of Gibbs free energy for adsorption of benzotriazole, 2-mercaptobenzothiazole, 8-hydroxyquinoline, and 3-amino-1, 2, 4-triazole-5-thiol as corrosion inhibitors on the Al-Mg-Sn alloy surface in NaCl solution at 300K.

The adsorptive capacity of inhibitor structures on the Al-Mg-Sn alloy surface is approved by the ΔG^{o}_{ads} amounts: $\Delta G^{o}_{ads} = \Delta G^{o}_{inh\rightarrow[Al-Mg-Ge]} - \left(\Delta G^{o}_{inh} + \Delta G^{o}_{[Al-Mg-Ge]}\right)$ **(2)**

Based on the data in Table 1, it is predicted that the adsorption of the inhibitor on the Al-Mg-Sn alloy surface might be physical and chemical. As shown in Figure3, all the computed ΔG^{o}_{ads} amounts are very close, which exhibits the agreement of the evaluated data by all methods and the validity of the computations, and it has also represented the maximum fluctuation for benzotriazole → Al-Mg-Sn, 2-mercaptobenzothiazole → Al-Mg-Sn, 8-hydroxyquinoline → Al-Mg-Sn, and 3-amino-1, 2, 4-triazole-5-thiol → Al-Mg-Sn, respectively (Figure3). Moreover, 2-mercaptobenzothiazole → Al-Mg-Sn has shown a sharpest peak in ΔG^{o}_{ads} amount which displays the most stability in the coating process of the Al-Mg-Sn alloy surface with 2-mercaptobenzothiazole.

3.3. NMR analysis.

The atomic charge and NMR data of isotropic (σ_{iso}) and anisotropic shielding tensor (σ_{aniso}) for benzotriazole → Al-Mg-Sn, 2-mercaptobenzothiazole→ Al-Mg-Sn, 8-hydroxyquinoline → Al-Mg-Sn, and 3-amino-1, 2, 4-triazole-5-thiol → Al-Mg-Sn have been calculated using Gaussian 16 revision C.01 software [56] and reported in Tables 2.

The quantum chemical calculations yield the CS tensors in the principal axes system to evaluate the isotropic chemical shielding (CSI) and anisotropic chemical shielding (CSA) [68,69].

$\text{CSI (ppm)} = (\sigma 33 + \sigma 22 + \sigma 11)/3$; $\text{CSA (ppm)} = \sigma 33 - (\sigma 22 + \sigma 11)/2$ **(3)**

The nuclear magnetic resonance (NMR) calculation for chemical shifts for assigning the structural and geometrical of compounds has been accomplished. The Gauge Invariant Atomic Orbital (GIAO) method has been suggested as an accurate method for NMR parameter calculations, and ONIOM has obtained much attention for achieving NMR chemical shifts in inhibitor-surface complexes, for instance, isotropic chemical shielding becomes: $\sigma_{iso,ONIOM} = \sigma_{iso,high(QM1)} + \sigma_{iso,medium(QM2)} + \sigma_{iso,low(QM3)}$ **(4)**

Table 2. Atomic charge and NMR properties of some atoms of benzotriazole, 2-mercaptobenzothiazole, 8-hydroxyquinoline, and 3-amino-1, 2, 4-triazole-5-thiol in ppm adsorbed onto Al-Mg-Sn alloys surface.

Benzotriazole → Al-Mg-Sn				**2-mercaptobenzothiazole→ Al-Mg-Sn**			
Atom number	**σ CSI**	**σ CSA**	**Q**	**Atom number**	**σ CSI**	**σ CSA**	**Q**
C1	114.3719	111.5103	-0.0738	C1	135.4827	122.2164	-0.0023
C2	111.5103	136.3086	-0.0102	C2	134.0305	131.4802	-0.0116
C3	138.0351	126.4199	0.0242	C3	149.0780	100.2927	-0.2360
C4	106.3125	39.5747	0.0461	C4	133.0540	86.7858	0.0702
C5	130.3430	126.5741	0.0100	C5	134.2155	129.4327	0.0101
C6	122.3309	123.4682	-0.0164	C6	132.7376	131.7010	-0.0115
N7	57.2493	138.0711	-0.3121	S7	696.2436	250.0264	0.4793
N8	-8.7032	158.1511	-0.0885	C8	102.6308	89.7471	-0.2395
N9	38.7117	268.2512	-0.1645	N9	75.4570	335.9681	-0.2897
Al10	702.1838	275.4445	0.0900	S10	-22.4094	856.1289	0.1571
Mg11	761.6685	267.4335	0.0316	Al11	391.1040	785.5949	0.0671
Sn12	4058.2518	1272.1525	0.4366	Mg12	806.6412	445.2140	0.1359
Mg13	399.8453	602.6138	0.2211	Sn13	4140.1786	1187.7955	0.3078
Al14	708.5994	252.5539	0.1079	Mg14	346.6557	584.6876	0.2036
Mg15	776.8065	323.8654	0.0487	Al15	540.4763	463.8311	0.0959
Al16	745.3716	652.7731	-1.0214	Mg16	792.1864	393.8883	0.0535
Sn17	4673.7162	1806.3341	1.2094	Al17	645.6761	655.8856	-1.2978
Al18	488.0733	1162.2418	-0.5660	Sn18	4592.0476	452.7741	0.9882
Sn19	4329.2655	1653.2828	0.4516	Al19	497.0951	693.2236	-0.5104
Mg20	440.5888	853.6722	0.1380	Sn20	4069.1022	1284.5960	0.3277
Al21	480.3819	829.5359	-0.5625	Mg21	149.7520	862.6473	0.2032
				Al22	448.5721	946.8021	-0.5009
8- hydroxyquinoline → Al-Mg-Sn				**3-amino-1, 2, 4-triazole-5-thiol → Al-Mg-Sn**			
Atom number	σ CSI	σ CSA	Q	Atom number	σ CSI	σ CSA	Q
C1	102.0569	111.9979	0.0830	N1	66.9264	247.6545	-0.3004
C2	131.0711	127.5903	-0.0211	C2	109.5954	92.3875	0.2183
C3	121.7130	116.8377	0.0412	C3	119.1594	81.1483	-0.0091
C4	127.4688	156.8578	-0.0089	N4	94.4527	129.7761	-0.0103
C5	127.6067	122.4482	-0.0190	N5	58.4482	144.6040	-0.2182
C6	122.6465	138.8508	0.0018	N6	277.4899	35.4466	0.0489
N7	1.4167	514.1823	-0.2409	S7	265.9923	593.8397	0.2773
C8	112.9545	120.5671	0.0932	Al8	526.8810	562.0817	0.0873
C9	128.0123	137.0395	-0.0081	Mg9	798.6243	358.3865	0.0392
C10	121.5615	130.0987	0.0087	Sn10	3759.063	1774.650	0.2568
O11	-46.0293	158.6509	-0.2913	Mg11	440.4447	433.9357	0.1743
Al12	596.8899	322.3961	0.0727	Al12	711.3640	915.2915	0.0909
Mg13	781.2908	357.8333	0.0277	Mg13	815.4889	286.3621	-0.0347
Sn14	4153.8271	1769.5532	0.3997	Al14	827.2325	260.6616	-1.1620
Mg15	455.3760	744.8593	0.1930	Sn15	4543.4737	696.4354	0.9791
Al16	608.8907	271.1807	0.0631	Al16	597.8456	759.2739	-0.4844
Mg17	782.5814	367.1019	0.0587	Sn17	3922.8448	1228.676	0.2448
Al18	632.1691	649.1342	-1.0001	Mg18	393.4493	324.4752	0.2344
Sn19	4503.4789	817.2149	1.2268	Al19	564.5291	485.0830	-0.4324
Al20	700.5231	421.4249	-0.5863				
Sn21	4100.5769	1675.7585	0.2940				
Mg22	439.1576	724.9231	0.1955				
Al23	756.7260	423.5339	-0.5839				

Besides, the solution of NaCl solution has influenced the nuclear magnetic resonance data and chemical shielding of carbon, nitrogen, oxygen, sulfur, aluminum, magnesium, and silicon in benzotriazole → Al-Mg-Sn, 2-mercaptobenzothiazole → Al-Mg-Sn, 8-hydroxyquinoline → Al-Mg-Sn, and 3-amino-1, 2, 4-triazole-5-thiol → Al-Mg-Sn. In Figure 4, it has been indicated the chemical shielding tensors of isotropic (σ_{CSI}) and anisotropic (σ_{CSA}) of some effective atoms in the adsorption site of benzotriazole → Al-Mg-Sn, 2-mercaptobenzothiazole → Al-Mg-Sn, 8- hydroxyquinoline → Al-Mg-Sn, and 3-amino-1, 2, 4-triazole-5-thiol → Al-Mg-Sn (Table 2). Figure 4 has certainly focused on the aluminum shielding in the intra-atomic interaction with magnesium and silicon and simultaneously interatomic interaction with other atoms in organic inhibitors through various high, medium, and low layers of the ONIOM method.

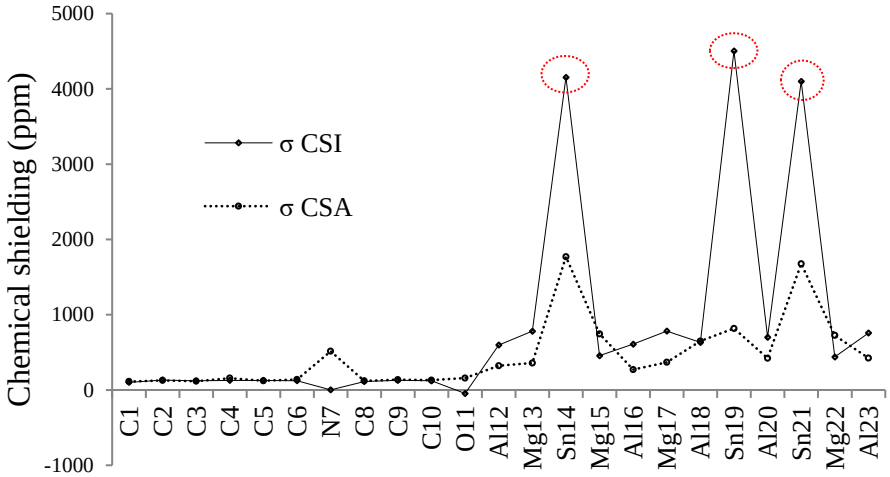

Figure 4. The NMR plot of isotropic (σ_{iso}) and anisotropic (σ_{aniso}) shielding tensors for aluminum through intra-atomic interaction with magnesium and silicon atoms in alloy surface of Al-Mg-Sn and interatomic interaction with organic inhibitors in the adsorption site of (N→ Al, O→Al, S→Al) calculated by level of theory CAM-B3LYP/6-31+G(d,p)/EPR-III/LANL2DZ.

Interatomic interactions, which are related to the position of one, two, three, etc. atoms at a time, are written as a series expansion of functional parameters with interatomic potential [68,69].

Where V_1 is the one-body term, V_2 the two-body term, V_3 the three-body term, N the number of atoms in the system, $\vec{r}_i$ the position of atom i, $\vec{r}_j$ the position of atom j , the position of atom k, and i, j, k are indices that sprain around atom positions.

In Figure 4, we have presented that the isotropic and anisotropy shielding increase with the occupancy and consequently, the negative charge of nitrogen, oxygen, and sulfur atoms in benzotriazole, 2-mercaptobenzothiazole, 8- hydroxyquinoline, and 3-amino-1, 2, 4-triazole-5-thiol diffusing onto Al-Mg-Sn alloy surface. It has been exhibited that the graph of nitrogen, oxygen, and sulfur atoms has the same attitude but a considerable deviation from that of carbon and hydrogen atoms.

Intra-atomic interactions consist of Al-Al, Al-Mg, Al-Sn, Mg-Mg, Mg-Sn, Sn-Sn and interatomic interaction are N → Al-Mg-Sn, O → Al-Mg-Sn, S→ Al-Mg-Sn based on the of CAM-B3LYP/6-31+G(d,p)/EPR-III/LANL2DZ quantum mechanics calculations using Gaussian 16 revision C.01 program (Figure 4).

Based on Figure 4, it has been observed that Al-Sn(14), Al-Sn(19), and Al-Sn(21) direct us to the most influence in the neighbor atoms generated by interatomic reactions of N→Al, O→ Al, S→ Al in the Al-Mg-Sn alloy surface.

3.4. Charge density analysis.

Through observing the intra/inter interactions between organic inhibitors of benzotriazole, 2-mercaptobenzothiazole, 8- hydroxyquinoline, and 3-amino-1, 2, 4-triazole-5-thiol with Al-Mg-Sn alloy surface and consequently formation of adsorbed surfaces of benzotriazole → Al-Mg-Sn, 2-mercaptobenzothiazole→ Al-Mg-Sn, 8- hydroxyquinoline → Al-Mg-Sn, and 3-amino-1, 2, 4-triazole-5-thiol → Al-Mg-Sn (Tables 2) based on Langmuir adsorption using CAM-B3LYP/6-31+G(d,p)/EPR-III/LANL2DZ level of theory, CDD (the charge density difference) for these structures at the adsorption site has been estimated and plotted in Figure 5 with the following equation: $\Delta Q_{ads} = Q_{inhibitor\rightarrow[Al-Mg-Sn]\,surface} - (Q_{inhibitor} + Q_{[Al-Mg-Sn]\,surface})$, where $Q_{inhibitor\rightarrow[Al-Mg-Sn]\,surface}$ is the charge density of the adsorption system; $Q_{inhibitor}$ and $Q_{[Al-Mg-Sn]surface}$ are the charge densities of non-interacting organic inhibitor and that of the Al-Mg-Sn alloy surface.

Figure 5. The calculated electronic charge for aluminum atom through intra-atomic interaction with magnesium and tin in the alloy surface of [Al-Mg-Sn] and through interatomic interaction with organic inhibitors in the adsorption site (N→ Al, O→Al, S→Al) calculated by the level of theory CAM-B3LYP/6-31+G (d,p)/EPR-III/LANL2DZ.

Furthermore, the charge density (Table 2) has shown a more important charge transfer from nitrogen, oxygen, and sulfur of benzotriazole, 2-mercaptobenzothiazole, 8-hydroxyquinoline, and 3-amino-1,2,4-triazole-5-thiol as the electron donor adsorbed onto Al–Mg–Sn nanoalloy surface which acts as the electron acceptor (N → Al, O → Al and S → Al). Al sites in Al–Mg–Sn nanoalloy surface have higher interaction energy from Van der Waals' forces with these heterocyclic inhibitors that can make them highly stable toward coating information on the surface.

It has been predicted that the priority for selecting the surface binding of nitrogen, oxygen, and sulfur of these heterocyclic inhibitors in adsorption sites can be affected by the presence of close atoms of magnesium and tin in the Al–Mg–Sn nanoalloy surface.

3.5. Nuclear quadrupole resonance (NQR).

Nuclear quadrupole resonance (NQR) frequency for benzotriazole → Al-Mg-Sn, 2-mercaptobenzothiazole → Al-Mg-Sn, 8- hydroxyquinoline → Al-Mg-Sn, and 3-amino-1, 2, 4-triazole-5-thiol Al-Mg-Sn is proportional to the product of the nuclear quadrupole moment, a property of the nucleus, and the EFG in the neighborhood of the nucleus. As the EFG at the position of the nucleus in organic inhibitors is assigned by the valence electrons twisted in the special linkage with close nuclei of aluminum surface, the NQR frequency at which transitions happen is particular for an inhibitor→ metal alloy complex (Table 2). In NMR, nuclei with spin≥ 1/2 have a magnetic dipole moment so that their energies are split by a magnetic field, permitting resonance sorption of energy dependent on the Larmor frequency; $\omega_L = \gamma B$, where γ is the gyromagnetic ratio, and B is the magnetic field external to the nucleus [70-72]. NQR nuclei with spin≥ 1 have an electric quadrupole moment, accompanied by non-spherical nuclear charge distributions. So, the nuclear charge distribution deviates from that of a sphere as the oblate or prolate form of the nucleus.

NQR is a straight frame of the interaction of the quadrupole moment with the local electric field gradient (EFG), which is produced by the electronic structure of its ambiance.

In this article, the electric potential as the amount of work energy through transferring the electric charge from one site to another site in the presence of an electric field has been measured for benzotriazole, 2-mercaptobenzothiazole, 8- hydroxyquinoline, and 3-amino-1, 2, 4-triazole-5-thiol diffusing onto Al-Mg-Sn alloy surface using CAM-B3LYP/EPR-III,LANL2DZ,6-31+G(d,p) level of theory (Table 3).

Table 3. The electric potential for elements of benzotriazole, 2-mercaptobenzothiazole, 8-hydroxyquinoline, and 3-amino-1, 2, 4-triazole-5-thiol adsorbed on the Al-Mg-Sn alloy surface by CAM-B3LYP/EPR-III,6-31+G(d,p) calculation extracted of NQR method.

Atom type	Benzotriazole	Atom type	2-mercapto benzothiazole	Atom type	8- hydroxy quinoline	Atom type	3-amino-1, 2, 4-triazole-5-thiol
C1	-14.6086	C1	-14.5618	C1	-14.5076	N1	-18.1769
C2	-14.5697	C2	-14.5712	C2	-14.5653	C2	-14.484
C3	-14.5252	C3	-14.5685	C3	-14.5284	C3	-14.5521
C4	-14.5395	C4	-14.5404	C4	-14.5463	N4	-18.0548
C5	-14.5607	C5	-14.5722	C5	-14.5725	N5	-18.1677
C6	-14.5724	C6	-14.5727	C6	-14.5583	N6	-18.0486
N7	-18.0932	S7	-58.284	N7	-18.1174	S7	-58.3092
N8	-18.0873	C8	-14.6011	C8	-14.5255	Al8	-43.692
N9	-18.0993	N9	-18.1452	C9	-14.5573	Mg9	-38.648
Al10	-43.6865	S10	-58.4102	C10	-14.5516	Sn10	-283.425
Mg11	-38.6191	Al11	-43.6986	O11	-22.0603	Mg11	-38.856
Sn12	-283.404	Mg12	-38.5954	Al12	-43.7041	Al12	-43.6988
Mg13	-38.8472	Sn13	-283.408	Mg13	-38.634	Mg13	-38.5987
Al14	-43.6827	Mg14	-38.8678	Sn14	-283.42	Al14	-43.1135
Mg15	-38.6199	Al15	-43.6959	Mg15	-38.8648	Sn15	-283.154
Al16	-43.146	Mg16	-38.6397	Al16	-43.7076	Al16	-43.4141
Sn17	-283.136	Al17	-43.1639	Mg17	-38.6351	Sn17	-283.426
Al18	-43.4308	Sn18	-283.154	Al18	-43.1525	Mg18	-38.8743
Sn19	-283.394	Al19	-43.4422	Sn19	-283.148	Al19	-43.4389

Atom type	Benzotriazole	Atom type	2-mercapto benzothiazole	Atom type	8- hydroxy quinoline	Atom type	3-amino-1, 2, 4-triazole-5-thiol
Mg20	-38.8398	Sn20	-283.416	Al20	-43.4441		
Al21	-43.438	Mg21	-38.8631	Sn21	-283.422		
		Al22	-43.4417	Mg22	-38.8666		
				Al23	-43.4456		

In addition, in Figure 6a-d, it has been plotted the electric potential of NQR method for elements of benzotriazole, 2-mercaptobenzothiazole, 8- hydroxyquinoline, and 3-amino-1, 2, 4-triazole-5-thiol that have been adsorbed on the Al-Mg-Sn alloy surface using CAM-B3LYP/EPR-III, LANL2DZ,6-31+G(d,p) level of theory.

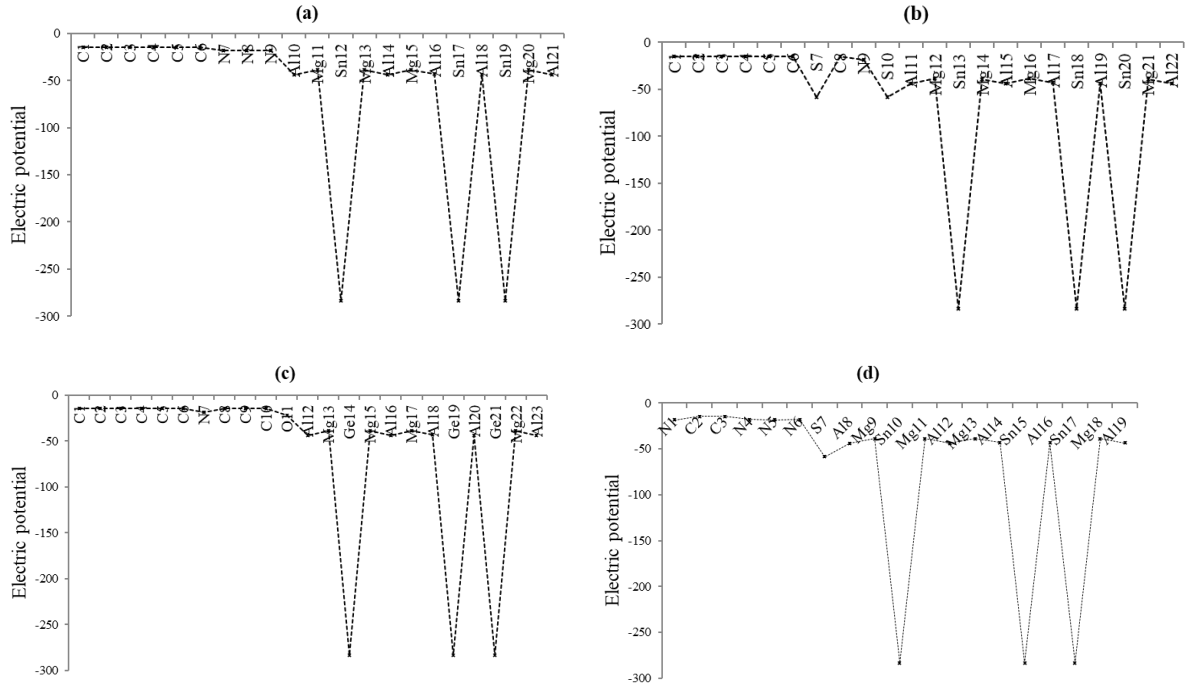

Figure 6. The electric potential versus atom number through NQR calculation for **a)** benzotriazole; **b)** 2-mercaptobenzothiazole; **c)** 8-hydroxyquinoline;**d)** 3-amino-1, 2, 4-triazole-5-thiol adsorbing on the Al-Mg-Sn alloy surface using CAM-B3LYP/EPR-III, LANL2DZ,6-31+G(d,p).

Therefore, it has been observed the effect of the substitution of aluminum atoms in Al-Al surface with magnesium and tin in the aluminum alloy (Al-Mg-Sn) through the resulted electric potential using NQR analysis (Figure 6). It's obvious that the graph of Al-Al fluctuates by Mg and Sn atoms in the related alloy. In Figure 6, it has been remarked the changes of electric potential for carbon, nitrogen, oxygen, sulfur, aluminum, magnesium, and tin in benzotriazole → Al-Mg-Sn, 2-mercaptobenzothiazole→ Al-Mg-Sn, 8- hydroxyquinoline → Al-Mg-Sn, and 3-amino-1, 2, 4-triazole-5-thiol → Al-Mg-Sn.

3.6. Potential energy of interatomic interaction.

The interatomic potential explains the interaction between a pair of atoms or the interaction of an atom with a group of atoms in a condensed phase. When binding happens, we can observe the potential to have both an attractive and a repulsive component. The figure of the potential energy as a function of lattice distance with the interval of interatomic interaction in a solid describes that an atom in the ideal crystalline solid feels the same potential through the other atoms in the material. It investigated the Morse potential, which is applied to molecular vibrations and solids, and also excited the functional form of more accurate potentials like the bond-order potentials [73].

Where D_e is the equilibrium bond energy and r_e the bond distance. Therefore, the optimized potential energy of interatomic interaction for benzotriazole → Al-Mg-Sn, 2-mercaptobenzothiazole→ Al-Mg-Sn, 8- hydroxyquinoline → Al-Mg-Sn, and 3-amino-1, 2, 4-triazole-5-thiol → Al-Mg-Sn have been measured (Table 4).

Table 4. Potential energy (kcal/mol) of interatomic interaction and distance (Å) of a nitrogen atom in benzotriazole, oxygen atom in 8- hydroxyquinoline, and sulfur atom in both 2-mercaptobenzothiazole and 3-amino-1, 2, 4-triazole-5-thiol, respectively, with aluminum in Al-Mg-Sn nanosurface.

Compound	**Potential energy×10^{-5} (kcal/mol)**	**Distance**	**(Å)**
Al-Mg-Sn	-124.6274	-	-
Benzotriazole	-24.5172	-	-
Benzotriazole → Al-Mg-Sn	-127.0736	$N_{inhibitor}$ → $Al_{surface}$	2.0034
2-mercaptobenzothiazole	-69.5235	-	-
2-mercaptobenzothiazole→ Al-Mg-Sn	-131.5725	$S_{inhibitor}$ → $Al_{surface}$	2.1999
8- hydroxyquinoline	-29.5527	-	-
8- hydroxyquinoline → Al-Mg-Sn	-127.5784	$O_{inhibitor}$ → $Al_{surface}$	1.9098
3-amino-1, 2, 4-triazole-5-thiol	-43.1337	-	-
3-amino-1, 2, 4-triazole-5-thiol → Al-Mg-Sn	-128.9338	$S_{inhibitor}$ → $Al_{surface}$	2.1999

Then, the distance between the nitrogen atom in benzotriazole, oxygen atom in 8-hydroxyquinoline, and sulfur atom in both 2-mercaptobenzothiazole and 3-amino-1, 2, 4-triazole-5-thiol, respectively, with aluminum in Al-Mg-Sn nanosurface has been evaluated (Table 4). Finally, the changes in potential energy for these complexes and interatomic integration distance have been plotted in Figure 7.

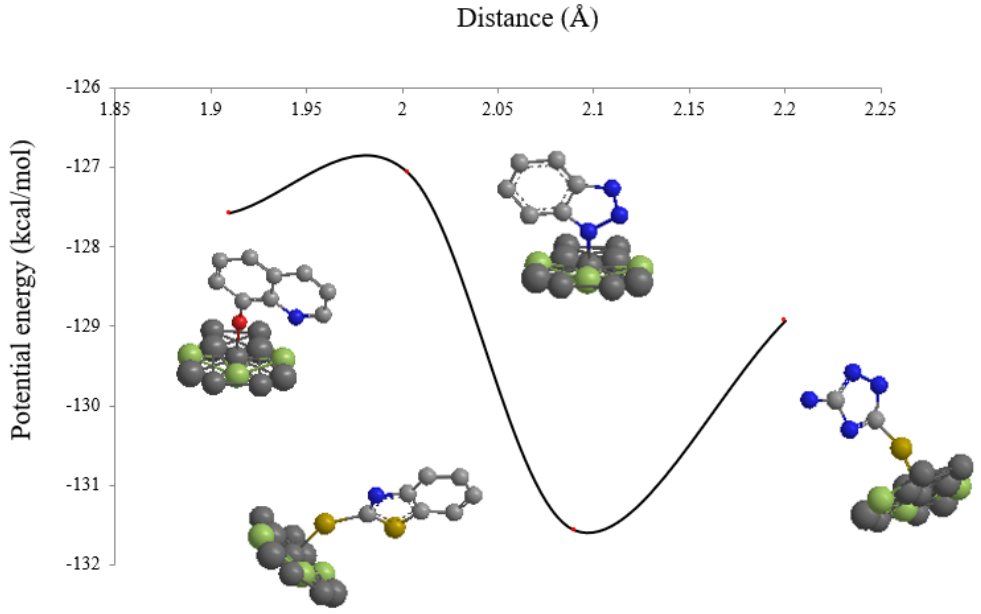

Figure 7. The graph of potential energy (kcal/mol) of interatomic interaction versus distance (Å) of a nitrogen atom in benzotriazole, the oxygen atom in 8- hydroxyquinoline, and the sulfur atom in both 2-mercaptobenzothiazole and 3-amino-1, 2, 4-triazole-5-thiol, respectively, with aluminum in Al-Mg-Sn nanosurface.

Based on Figure 7, it can be assumed that for benzotriazole → Al-Mg-Sn, 2-mercaptobenzothiazole→ Al-Mg-Sn, 8- hydroxyquinoline → Al-Mg-Sn, and 3-amino-1, 2, 4-triazole-5-thiol → Al-Mg-Sn, Lennar Jones potential as an intermolecular pair potential [74].

Where ε is the depth of the potential well, and σ is the interval at which the potential=0. The attractive term is proportional to $\frac{1}{r^6}$ in the potential comes from balancing the van der Waals forces, while the $\frac{1}{r^{12}}$ repulsive term is much more approximate [73,74].

3.7. HOMO, LUMO, and UV-VIS analysis.

The ionization causes the highest occupied molecular orbital (HOMO) energy and the electron affinity produces the lowest unoccupied molecular orbital (LUMO) energy which has been calculated and reported for benzotriazole → Al-Mg-Sn, 2-mercaptobenzothiazole → Al-Mg-Sn, 8- hydroxyquinoline → Al-Mg-Sn, and 3-amino-1, 2, 4-triazole-5-thiol → Al-Mg-Sn in Scheme 3. The HOMO (au), LUMO (au), and band energy gap ($\Delta E = E_{LUMO} - E_{HOMO}$) (ev) presented the pictorial explanation of the frontier molecular orbital and their respective positive and negative zones, which are an important factor for identifying the molecular characteristics of effective compounds in these organic inhibitors (Scheme 3).

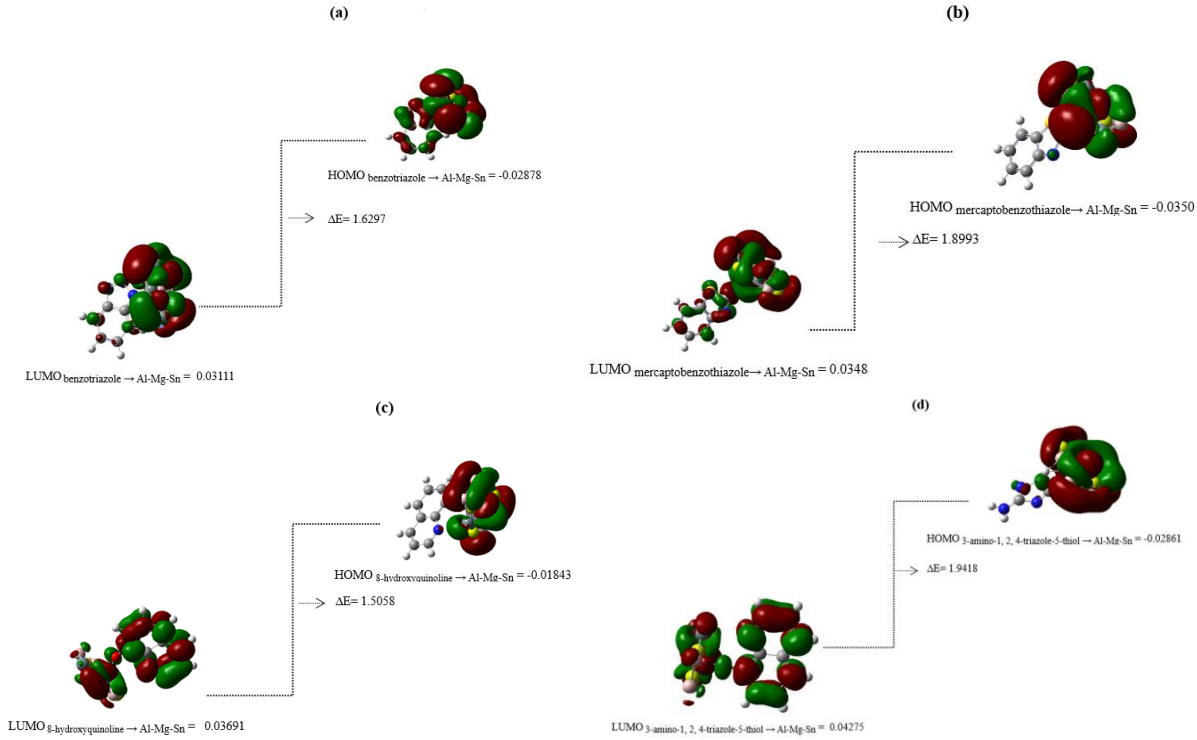

Scheme3. The HOMO, LUMO, and band energy gap (ev) for three organic inhibitors for **a)** benzotriazole → Al-Mg-Sn; **b)** 2-mercaptobenzothiazole; **c)** 8-hydroxyquinoline; **d)** 3-amino-1, 2, 4-triazole-5-thiol → Al-Mg-Sn.

On the other hand, the HOMO shows the capability for giving an electron while the LUMO as an electron acceptor, exhibits the capability for achieving an electron. Therefore, the energy gap ($\Delta E = E_{LUMO} - E_{HOMO}$) indicates the energy difference between frontier HOMO and LUMO orbital, introducing the stability for the structure and unraveling the chemical activity of the molecule. In this work, the energy gap establishes how benzotriazole, 8-hydroxyquinoline, 2-mercaptobenzothiazole, and 3-amino-1, 2, 4-triazole-5-thiol adsorb on the Al-Mg-Sn alloy surface at CAM-B3LYP/6-311+G(2d,p)/EPR-III/LANL2DZ quantum method. Besides, frontier molecular orbitals have important functions in the optical and electrical properties, such as in UV-VIS spectra [75].

The energy gap between HOMO and LUMO has distinguished the attributes of molecular electrical transport [76–79]. Through the Frank–Condon principle, the maximum absorption peak (max) depends on a UV–visible spectrum to vertical excitation.

In this verdict, TD-DFT/6-31+G (2d, p)/EPR-III/LANL2DZ computations have been done to identify the low-lying excited states of benzotriazole, 8-hydroxyquinoline, 2-mercaptobenzothiazole and 3-amino-1, 2, 4-triazole-5-thiol adsorbing on the Al-Mg-Sn alloy surface. The results consist of the vertical excitation energies, oscillator strength, and wavelength, introduced in Figure 8 a-d.

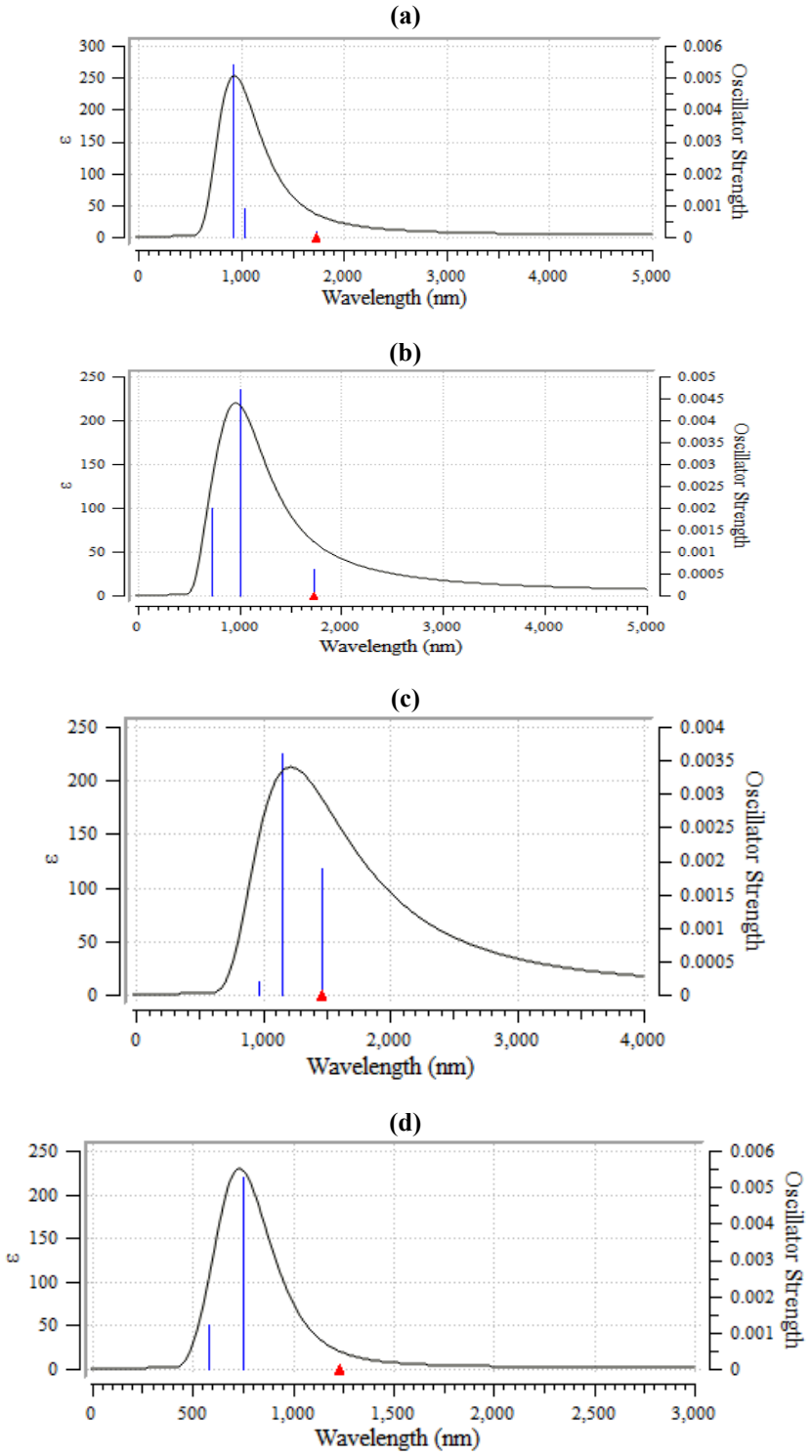

Figure 8. UV-VIS spectra for **a)** benzotriazole → Al-Mg-Sn; **b)** 2-mercaptobenzothiazole; **c)** 8-hydroxyquinoline; **d)** 3-amino-1, 2, 4-triazole-5-thiol → Al-Mg-Sn.

Based on the computed amounts of UV-VIS spectra for benzotriazole, 2-mercaptobenzothiazole, 8-hydroxyquinoline, and 3-amino-1, 2, 4-triazole-5-thiol adsorbing on the Al-Mg-Sn alloy surface, there are maximum adsorption bands between 500nm-2000nm wavelengths for these organic heterocyclic inhibitors joint metal alloy which has remarked a sharp peak with approximately 1000nm wavelength (Figure 8a-d).

4. Conclusions

In this research, the adsorption and diffusion of benzotriazole, 2-mercaptobenzothiazole, 8-hydroxyquinoline, and 3-amino-1, 2, 4-triazole-5-thiol adsorbing on the Al-Mg-Sn alloy surface have been investigated based on Langmuir theory using ONIOM method with high, medium and low levels of EPR-III/6-31+G (d,p)/LANL2DZ, semi-empirical and MM2 basis sets, respectively by program package Gaussian 16 revision C.01.

In this work, the efficiency of the organic inhibitors as the aluminum alloy coating has been studied through the electronic, thermodynamic features and characteristics of the environmental condition, which results in the complexes of benzotriazole → Al-Mg-Sn, 2-mercaptobenzothiazole → Al-Mg-Sn, 8- hydroxyquinoline → Al-Mg-Sn, and 3-amino-1, 2, 4-triazole-5-thiol → Al-Mg-Sn.

An elaborate investigation for the mechanism of local minima in the adsorption potential energy landscape represents that the intact benzotriazole, 2-mercaptobenzothiazole, 8-hydroxyquinoline, and 3-amino-1, 2, 4-triazole-5-thiol have been adsorbed with the aromatic ring parallel to the Al-Mg-Sn alloy surface. In the preferred path, these organic inhibitors remain parallel to the surface while performing small single rotational steps with a carbon-carbon double bond hinged above a single Al atom.

Funding

This research received no external funding.

Acknowledgments

In completing this paper and the research behind it, the corresponding author is grateful to all the authors for their helpful contributions.

Conflicts of Interest

The authors declare no conflict of interest.

References

1. Lu, L.; Qin, M.; Jia, X.; Wang, Z.; Chen, Q.; Sun, J.; Jiao, S. Experimental Study on the Thermal Stability of Aluminum Alloy 7075-T651 Structural Parts after Rolling Correction. *Metals* **2023**, *13*, 213, https://doi.org/10.3390/met13020213.
2. Mollaamin, F.; Monajjemi, M. Molecular modeling framework of metal-organic clusters for conserving surfaces: Langmuir sorption through the TD-DFT/ONIOM approach. *Mol. Simul.* **2023**, *49*, 365–376, https://doi.org/10.1080/08927022.2022.2159996.
3. Zupanič, F.; Macerl, M.; Haga, T.; Bončina, T. Microstructure and Indentation Properties of Single-Roll and Twin-Roll Casting of a Quasicrystal-Forming Al-Mn-Cu-Be Alloy. *Metals* **2022**, *12*, 187, https://doi.org/10.3390/met12020187.

4. Mollaamin, F.; Monajjemi, M. In Silico-DFT Investigation of Nanocluster Alloys of Al-(Mg, Ge, Sn) Coated by Nitrogen Heterocyclic Carbenes as Corrosion Inhibitors. *J. Clust. Sci*. **2023**, *34*, 2901-2918, https://doi.org/10.1007/s10876-023-02436-5.
5. Zhang, R.; Chiang, R.; Ren, Z.; Zhang, H.; Zhao, W.; Wang, G.-X.; Vasudevan, V.K.; Dong, Y.; Ye, C. Fatigue Performance Improvement of 7075-T651 Aluminum Alloy by Ultrasonic Nanocrystal Surface Modification. *J. Mater. Eng.Perform*. **2022**, *31*, 2354–2363, https://doi.org/10.1007/s11665-021-06308-9.
6. Mollaamin, F.; Shahriari, S.; Monajjemi, M.; Khalaj, Z. Nanocluster of Aluminum Lattice via Organic Inhibitors Coating: A Study of Freundlich Adsorption. *J. Clust. Sci.* **2023**, *34*, 1547–1562, https://doi.org/10.1007/s10876-022-02335-1.
7. Liu, W.; He, W.; Liu, L.; Li, J.; Pan, H.; Zhang, W.; Wang, Z. Microstructure and Tribological Properties of 7075-T651 Aluminum Alloy Affected by N-Ion Implantation. *J. Mater. Eng. Perform.* **2023**, *32*, 2007–2015, https://doi.org/10.1007/s11665-022-07219-z.
8. Martucci, A.; Aversa, A.; Lombardi, M. Ongoing Challenges of Laser-Based Powder Bed Fusion Processing of Al Alloys and Potential Solutions from the Literature—A Review. *Materials* **2023**, *16*, 1084, https://doi.org/10.3390/ma16031084.
9. Monajjemi, M.; Khaleghian, M.; Tadayonpour, N.; Mollaamin, F. THE EFFECT OF DIFFERENT SOLVENTS AND TEMPERATURES ON STABILITY OF SINGLE-WALLED CARBON NANOTUBE: A QM/MD STUDY. *Int. J. Nanosci*. **2010**, *9*, 517–529, https://doi.org/10.1142/S0219581X10007071.
10. Mollaamin, F.; Monajjemi,M. Adsorption ability of Ga_5N_{10} nanomaterial for removing metal ions contamination from drinking water by DFT, *Int J Quantum Chem* **2024**, *124*, e27348. https://doi.org/10.1002/qua.27348.
11. Khalili Hadad, B.; Mollaamin, F.; Monajjemi, M. Biophysical chemistry of macrocycles for drug delivery: A theoretical study. *Russ. Chem. Bull.* **2011**, *60*, 238-241, https://doi.org/10.1007/s11172-011-0039-5.
12. Šmalc, J.; Vončina, M.; Mrvar, P.; Balaško, T.; Krutiš, V.; Petrič, M. The Influence of Foundry Scrap Returns on Chemical Composition and Microstructure Development of AlSi9Cu3 Alloy. *Crystals* **2023**, *13*, 757, https://doi.org/10.3390/cryst13050757.
13. Mollaamin, F.; Monajjemi, M. In Situ Ti-Embedded SiC as Chemiresistive Nanosensor for Safety Monitoring of CO, CO_2, NO, NO_2: Molecular Modelling by Conceptual Density Functional Theory, *Russ. J. Phys. Chem. B*, **2024**, *18* (1), 49–66. https://doi.org/10.1134/S1990793124010159.
14. Lu, Y.; Wu, C.; Wu, H.; Wang, J.; Su, Y.; Gan, Z.; Liu, J. Growth Mechanism of Eutectic Si in Super-Gravity Solidified Al-Si Alloy during Annealing. *Crystals* **2023**, *13*, 684, https://doi.org/10.3390/cryst13040684.
15. Mollaamin, F.; Monajjemi, M.; Salemi, S.; Baei, M.T. A Dielectric Effect on Normal Mode Analysis and Symmetry of BNNT Nanotube. *Fuller. Nanotub. Carbon Nanostructures* **2011**, *19*, 182–196, https://doi.org/10.1080/15363831003782932.
16. Monajjemi, M.; Mahdavian, L.; Mollaamin, F.; Khaleghian, M. Interaction of Na, Mg, Al, Si with carbon nanotube (CNT): NMR and IR study. *Russ. J. Inorg. Chem*. **2009**, *54*, 1465-1473, https://doi.org/10.1134/S0036023609090216.
17. Bakhshi, K.; Mollaamin, F.; Monajjemi, M. Exchange and Correlation Effect of Hydrogen Chemisorption on Nano V(100) Surface: A DFT Study by Generalized Gradient Approximation (GGA). *J. Comput. Theor. Nanosci*. **2011**, *8*, 763–768, https://doi.org/10.1166/jctn.2011.1750.
18. Mollaamin, F.; Ilkhani, A.; Sakhaei, N.; Bonsakhteh, B.; Faridchehr, A.; Tohidi, S.; Monajjemi, M. Thermodynamic and Solvent Effect on Dynamic Structures of Nano Bilayer-Cell Membrane: Hydrogen Bonding Study. *J. Comput. Theor. Nanosci.* **2015**, *12*, 3148–3154, https://doi.org/10.1166/jctn.2015.4092.
19. Hirsch, S.J.; Grund, T.; Lampke, T. Towards Closed-Loop Recycling of Ceramic Particle-Reinforced Aluminium Alloys: Comparative Study of Resistance-Heating Sintered Primary and Solid-State Recycled Secondary SiC_p/AlSi7Mg Composites. *Crystals* **2023**, *13*, 830, https://doi.org/10.3390/cryst13050830.
20. Hirsch, S.J.; Eiselt, P.; Ozdemir, I.; Grund, T.; Nestler, A.; Lampke, T.; Schubert, A. Investigation of the Tribological Behaviour of Various AMC Surfaces against Brake Lining Material. *Materials* **2023**, *16*, 1001, https://doi.org/10.3390/ma16031001.
21. Boughoues, Y.; Benamira, M.; Messaadia, L.; Ribouh, N. Adsorption and corrosion inhibition performance of some environmental friendly organic inhibitors for mild steel in HCl solution via experimental and theoretical study. *Colloids Surf. A Physicochem. Eng. Asp.* **2020**, *593*, 124610, https://doi.org/10.1016/j.colsurfa.2020.124610.

22. Özcan, M.; Solmaz, R.; Kardaş, G.; Dehri, İ. Adsorption properties of barbiturates as green corrosion inhibitors on mild steel in phosphoric acid. *Colloids Surf. A Physicochem. Eng. Asp.* **2008**, *325*, 57–63, https://doi.org/10.1016/j.colsurfa.2008.04.031.
23. Saranya, J.; Sowmiya, M.; Sounthari, P.; Parameswari, K.; Chitra, S.; Senthilkumar, K. N-heterocycles as corrosion inhibitors for mild steel in acid medium. *J. Mol. Liq.* **2016**, *216*, 42-52, https://doi.org/10.1016/j.molliq.2015.12.096.
24. Mollaamin, F. Computational Methods in the Drug Delivery of Carbon Nanocarriers onto Several Compounds in Sarraceniaceae Medicinal Plant as Monkeypox Therapy. *Computation* **2023**, *11*, 84, https://doi.org/10.3390/computation11040084.
25. Özcan, M.; Karadağ, F.; Dehri, I. Interfacial Behavior of Cysteine between Mild Steel and Sulfuric Acid as Corrosion Inhibitor. *Acta Phys-Chim. Sin.* **2008**, *24*, 1387–1392, https://doi.org/10.1016/S1872-1508(08)60059-5.
26. Mobin, M.; Aslam, R. Experimental and theoretical study on corrosion inhibition performance of environmentally benign non-ionic surfactants for mild steel in 3.5% NaCl solution. *Process Saf. Environ. Prot.* **2018**, *114*, 279–295, https://doi.org/10.1016/j.psep.2018.01.001.
27. Singh, A.; Lin, Y.; Quraishi, M.A.; Olasunkanmi, L.O.; Fayemi, O.E.; Sasikumar, Y.; Ramaganthan, B.; Bahadur, I.; Obot, I.B.; Adekunle, A.S.; Kabanda, M.M.; Ebenso, E.E. Porphyrins as Corrosion Inhibitors for N80 Steel in 3.5% NaCl Solution: Electrochemical, Quantum Chemical, QSAR and Monte Carlo Simulations Studies. *Molecules* **2015**, *20*, 15122-15146, https://doi.org/10.3390/molecules200815122.
28. Ali, S.A.; Mazumder, M.A.J.; Nazal, M.K.; Al-Muallem, H.A. Assembly of succinic acid and isoxazolidine motifs in a single entity to mitigate CO_2 corrosion of mild steel in saline media. *Arab. J. Chem.* **2020**, *13*, 242–257, https://doi.org/10.1016/j.arabjc.2017.04.005.
29. Amar, H.; Benzakour, J.; Derja, A.; Villemin, D.; Moreau, B. A corrosion inhibition study of iron by phosphonic acids in sodium chloride solution. *J. Electroanal. Chem.* **2003**, *558*, 131–139, https://doi.org/10.1016/S0022-0728(03)00388-7.
30. Sherif, E.-S.M. A Comparative Study on the Electrochemical Corrosion Behavior of Iron and X-65 Steel in 4.0 wt % Sodium Chloride Solution after Different Exposure Intervals. *Molecules* **2014**, *19*, 9962–9974, https://doi.org/10.3390/molecules19079962.
31. Yang, D.; Zhang, M.; Zheng, J.; Castaneda, H. Corrosion inhibition of mild steel by an imidazolium ionic liquid compound: the effect of pH and surface pre-corrosion. *RSC Adv.* **2015**, *5*, 95160-95170, https://doi.org/10.1039/C5RA14556B.
32. Mollaamin, F. Phenolic Compounds in Black Grape by the Electronic and Thermochemical Studies. *Biointerface Res. Appl. Chem.* **2023**, *13*, 162, https://doi.org/10.33263/BRIAC132.162.
33. Monajjemi, M.; Mollaamin, F. BNB-BnNn Nano-Motor in Binding with ACC (tRNA) Nucleotides as an Amino Acid Detector in Ribosome: QM/MM & Monte Carlo Studies. *Biointerface Res. Appl. Chem*. **2023**, *13*, 254, https://doi.org/10.33263/BRIAC133.254.
34. Mollaamin, F.; Monajjemi, M. Aging Genome Modification and Editing using the CrisprCas9 system: Anti-Alzheimer Study by Docking Methods. *Biointerface Res. Appl. Chem.* **2023**, *13*, 224, https://doi.org/10.33263/BRIAC133.224.
35. Mollaamina,F., Mohammadi,S., Khalaj, Z., Monajjemi,M., Computational Modelling of Boron Nitride Nanosheet for Detecting and Trapping of Water Contaminant, *Russ. J. Phys. Chem. B*, **2024**, *18* (1), 67–82. https://doi.org/10.1134/S1990793124010330.
36. Monajjemi, M.; Mollaamin, F.; Küçük, Ö. Removing Non-Biodegradable Toxic Ions via Bio-Oxidation Analysis in Anzali Lagoon: A Usage of Seaweed in Biodiversity. *Biointerface Res. Appl. Chem*. **2023**, *13*, 282, https://doi.org/10.33263/BRIAC133.282.
37. Amberchan, G.; Lopez, I.; Ehlke, B.; Barnett, J.; Bao, N.Y.; Allen, A.; Singaram, B.; Oliver, S.R.J. Aluminum Nanoparticles from a Ga–Al Composite for Water Splitting and Hydrogen Generation. *ACS Appl. Nano Mater.* **2022**, *5*, 2636-2643, https://doi.org/10.1021/acsanm.1c04331.
38. Mollaamin, F.; Monajjemi, M. Tailoring and functionalizing the graphitic-like GaN and GaP nanostructures as selective sensors for NO, NO_2, and NH_3 adsorbing: A DFT study. *J. Mol. Model.* **2023**, *29*, 170, https://doi.org/10.1007/s00894-023-05567-8.
39. Shahriari, S.; Mollaamin, F.; Monajjemi, M. Increasing the Performance of {[(1-x-y) $LiCo_{0.3}Cu_{0.7}$] (Al and Mg doped)] O_2}, xLi_2MnO_3, $yLiCoO_2$ Composites as Cathode Material in Lithium-Ion Battery: Synthesis and Characterization. *Micromachines* **2023**, *14*, 241, https://doi.org/10.3390/mi14020241.

40. Mollaamin, F.; Monajjemi, M. Transition metal (X = Mn, Fe, Co, Ni, Cu, Zn)-doped graphene as gas sensor for CO_2 and NO_2 detection: a molecular modeling framework by DFT perspective. *J. Mol. Model*. **2023**, *29*, 119, https://doi.org/10.1007/s00894-023-05526-3.
41. Mashuga, M.E.; Olasunkanmi, L.O.; Ebenso, E.E. Experimental and theoretical investigation of the inhibitory effect of new pyridazine derivatives for the corrosion of mild steel in 1M HCl. *J. Mol. Struct*. **2017**, *1136*, 127–139, https://doi.org/10.1016/j.molstruc.2017.02.002.
42. Guimarães, T.A.S.; da Cunha, J.N.; de Oliveira, G.A.; da Silva, T.U.; de Oliveira, S.M.; de Araújo, J.R.; Machado, S.d.P.; D'Elia, E.; Rezende, M.J.C. Nitrogenated derivatives of furfural as green corrosion inhibitors for mild steel in HCl solution. *J. Mater. Res. Technol*. **2020**, *9*, 7104-7122, https://doi.org/10.1016/j.jmrt.2020.05.019.
43. Mollaamin, F.; Monajjemi, M. Doping of Graphene Nanostructure with Iron, Nickel and Zinc as Selective Detector for the Toxic Gas Removal: A Density Functional Theory Study. *C* **2023**, *9*, 20, https://doi.org/10.3390/c9010020.
44. Tahan, A.; Mollaamin, F.; Monajjemi, M. Thermochemistry and NBO analysis of peptide bond: Investigation of basis sets and binding energy. *Russ. J. Phys. Chem. A* **2009**, *83*, 587–597, https://doi.org/10.1134/S003602440904013X.
45. Mollaamin, F.; Monajjemi, M. Corrosion Inhibiting by Some Organic Heterocyclic Inhibitors Through Langmuir Adsorption Mechanism on the Al-*X* (*X* = Mg/Ga/Si) Alloy Surface: A Study of Quantum Three-Layer Method of CAM-DFT/ONIOM. *J. Bio Tribo Corros.* **2023**, *9*, 33, https://doi.org/10.1007/s40735-023-00751-y.
46. Sarasia, E.M.; Afsharnezhad, S.; Honarparvar, B.; Mollaamin, F.; Monajjemi, M. Theoretical study of solvent effect on NMR shielding tensors of luciferin derivatives. *Phys. Chem. Liquids* **2011**, *49*, 561-571, https://doi.org/10.1080/00319101003698992.
47. Mollaamin, F.; Monajjemi, M. Tribocorrosion Framework of (Iron, Nickel, Zinc)-Doped Graphene Nanosheet: New Sights into Sulfur Dioxide and Hydrogen Sulfide Removal Using DFT/TD-DFT Methods. *J. Bio Tribo Corros.* **2023**, *9*, 47, https://doi.org/10.1007/s40735-023-00768-3.
48. Brandt, F.; Jacob, C.R. Systematic QM Region Construction in QM/MM Calculations Based on Uncertainty Quantification. *J. Chem. Theory Comput.* **2022**, *18*, 2584-2596, https://doi.org/10.1021/acs.jctc.1c01093.
49. Mollaamin, F.; Özcan, S.; Özcan, E.; Monajjemi, M. Biomedical Applications of Bisphosphonate Chelating Agents by Metal Cations as Drug Design for Prevention and Treatment of Osteoporosis using QM/MM Method. *Biointerface Res. Appl. Chem*. **2023**, *13*, 329, https://doi.org/10.33263/BRIAC134.329.
50. Shahriari, S.; Zare, K.; Mollaamin, F. Outlook of Covid-19 Curing through Structural and Electronic Properties of Natural Drugs. *Biointerface Res. Appl. Chem*. **2023**, *13*, 345, https://doi.org/10.33263/BRIAC134.345.
51. Mollaamin, F.; Zare, K.; Shahriari, S. Delivery of some Trapped Metal Elements in the Boron Nitride Nanocone: Application of Bio-Sensors in Cell Membrane using a DFT Evaluation. *Biointerface Res. Appl. Chem*. **2023**, *13*, 542.
52. Khaleghian, M.; Zahmatkesh, M.; Mollaamin, F.; Monajjemi, M. Investigation of Solvent Effects on Armchair Single-Walled Carbon Nanotubes: A QM/MD Study. *Fuller. Nanotub. Carbon Nanostructures.* **2011**, *19*, 251-261, https://doi.org/10.1080/15363831003721757.
53. Mollaamin, F.; Monajjemi, M.; Küçük, Ö. Polymer Materials & Waste Industrial Products might be Dangerous for Destroying the Forests in Türkiye: An Overview of Climate Changing in Viewpoint of Bio Thermochemical Analysis. *Biointerface Res. Appl. Chem*. **2022**, *13*, 523, https://doi.org/1.33263/BRIAC136.523.
54. Mollaamin, F.; Monajjemi, M.; Naeimi, M.; Zare, K. Investigation on Controlling Therapy of Bone Skeletal and Marrow Cancer: A Biophysical Chemistry and Molecular Dynamic Study of Bisphosphonates Interaction with Bone Structures. *Biointerface Res. Appl. Chem*. **2023**, *13*, 396, https://doi.org/10.33263/BRIAC134.396.
55. Dennington, R.; Keith, T.A.; Millam, J.M. GaussView, Version 6, Semichem Inc., Shawnee Mission, KS, **2016**.
56. Frisch, M.J.; Trucks, G.W.; Schlegel, H.B.; Scuseria, G.E.; Robb, M.A.; Cheeseman, J.R.; Scalmani, G.; Barone, V.; Petersson, G.A.; Nakatsuji, H.; Li, X.; Caricato, M.; Marenich, A.V.; Bloino, J.; Janesko, B.G.; Gomperts, R.; Mennucci, B.; Hratchian, H.P.; Ortiz, J.V.; Izmaylov, A.F.; Sonnenberg, J.L.; Williams-Young, D.; Ding, F.; Lipparini, F.; Egidi, F.; Goings, J.; Peng, B.; Petrone, A.; Henderson, T.; Ranasinghe, D.; Zakrzewski, V.G.; Gao, J.; Rega, N.; Zheng, G.; Liang, W.; Hada, M.; Ehara, M.; Toyota, K.; Fukuda, R.;

Hasegawa, J.; Ishida, M.; Nakajima, T.; Honda, Y.; Kitao, O.; Nakai, H.; Vreven, T.; Throssell, K.; Montgomery Jr., J.A.; Peralta, J.E.; Ogliaro, F.; Bearpark, M.J.; Heyd, J.J.; Brothers, E.N.; Kudin, K.N.; Staroverov, V.N.; Keith, T.A.; Kobayashi, R.; Normand, J.; Raghavachari, K.; Rendell, A.P.; Burant, J.C.; Iyengar, S.S.; Tomasi, J.; Cossi, M.; Millam, J.M.; Klene, M.; Adamo, C.; Cammi, R.; Ochterski, J.W.; Martin, R.L.; Morokuma, K.; Farkas, O.; Foresman, J.B.; Fox, D.J. Gaussian 16, Revision C.01, Gaussian, Inc., Wallingford CT, **2016**.

57. Bilić, A.; Reimers, J.R.; Hush, N.S. Adsorption of Pyridine on the Gold(111) Surface: Implications for "Alligator Clips" for Molecular Wires. *J. Phys. Chem. B* **2002**, *106*, 6740-6747, https://doi.org/10.1021/jp020590i.
58. Malone, W.; Kara, A. A coverage dependent study of the adsorption of pyridine on the (111) coinage metal surfaces. *Surf. Sci.* **2020**, *693*, 121525, https://doi.org/10.1016/j.susc.2019.121525.
59. Monajjemi, M.; Mollaamin, F.; Gholami, M.R.; Yoosbashizadeh, H.; Sadrnezhad, S.K.; Passdar, H. Quantum Chemical Parameters of Some Organic Corrosion Inhibitors, Pyridine, 2-Picoline 4-Picoline and 2,4- Lutidine, Adsorption at Aluminum Surface in Hydrocholoric and Nitric Acids and Comparison Between Two Acidic Media. *Main Group Met. Chem.* **2003**, *26*, 349–362, https://doi.org/10.1515/MGMC.2003.26.6.349.
60. Dumont, E.; De Bleye, C.; Haouchine, M.; Coïc, L.; Sacré, P.-Y.; Hubert, P.; Ziemons, E. Effect of the functionalisation agent on the surface-enhanced Raman scattering (SERS) spectrum: Case study of pyridine derivatives. *Spectrochim. Acta Part A: Mol. Biomol. Spectrosc.* **2020**, *233*, 118180, https://doi.org/10.1016/j.saa.2020.118180.
61. Mollenhauer, D.; Gaston, N.; Voloshina, E.; Paulus, B. Interaction of Pyridine Derivatives with a Gold (111) Surface as a Model for Adsorption to Large Nanoparticles. *J. Phys. Chem. C* **2013**, *117*, 4470-4479, https://doi.org/10.1021/jp309625h.
62. Isvoranu, C.; Wang, B.; Ataman, E.; Schulte, K.; Knudsen, J.; Andersen, J.N.; Bocquet, M.-L.; Schnadt, J. Pyridine Adsorption on Single-Layer Iron Phthalocyanine on Au(111). *J. Phys. Chem. C* **2011**, *115*, 20201-20208, https://doi.org/10.1021/jp204460g.
63. Lee, C.; Yang, W.; Parr, R.G. Development of the Colle–Salvetti correlation-energy formula into a functional of the electron density. *Phys Rev B*. **1988**, *37*, 785, http://dx.doi.org/10.1103/PhysRevB.37.785.
64. Mollaamin, F.; Monajjemi, M. Trapping of toxic heavy metals from water by GN–nanocage: Application of nanomaterials for contaminant removal technique. *J. Mol. Struct* **2024**, *1300*, 137214. https://doi.org/10.1016/j.molstruc.2023.137214.
65. Mollaamin, F. Features of Parametric Point Nuclear Magnetic Resonance of Metals Implantation on Boron Nitride Nanotube by Density Functional Theory/Electron Paramagnetic Resonance. *Journal of Computational and Theoretical Nanoscience*. **2014**, *11*(11), 2393–2398. https://doi.org/10.1166/jctn.2014.3653.
66. Mollaamin, F.; Monajjemi, M. Harmonic Linear Combination and Normal Mode Analysis of Semiconductor Nanotubes Vibrations. *J. Comput. Theor. Nanosci* **2015**, *12*, 1030–1039, https://doi.org/10.1166/jctn.2015.3846.
67. Mollaamin, F.; Monajjemi, M. Electric and Magnetic Evaluation of Aluminum–Magnesium Nanoalloy Decorated with Germanium Through Heterocyclic Carbenes Adsorption: A Density Functional Theory Study. *Russ. J. Phys. Chem. B* **2023**, *17*, 658–672. https://doi.org/10.1134/S1990793123030223.
68. Finnis, M.W. Bond-order potentials through the ages. *Prog. Mater. Sci.* **2007**, *52*, 133–153, https://doi.org/10.1016/j.pmatsci.2006.10.003.
69. Monajjemi, M.; Baie, M.T.; Mollaamin, F. Interaction between threonine and cadmium cation in $[Cd(Thr)_n]^{2+}$ (n = 1–3) complexes: density functional calculations. *Russ. Chem. Bull.* **2010**, *59*, 886–889, https://doi.org/10.1007/s11172-010-0181-5.
70. Mollaamin, F.; Majid Monajjemi,M. HEXAGONAL HONEYCOMB PL-GaN NANOSHEET AS ADSORBENT SURFACE FOR GAS MOLECULES SENSING: A QUANTUM CHEMICAL STUDY, *Surface Review and Letters (SRL)*. **2024**, *31*(01), 1–14. https://doi.org/10.1142/S0218625X24500057.
71. Mollaamin, F.; Monajjemi, M. Graphene-based resistant sensor decorated with Mn, Co, Cu for nitric oxide detection: Langmuir adsorption & DFT method. *Sens. Rev.* **2023**, *43*, https://doi.org/10.1108/SR-03-2023-0040.
72. Mollaamin,F.; Majid Monajjemi,M. Molecular simulation of (Al–Ga) surface garnished with chromium metal for organic material detecting: A DFT study. *Functional Materials Letters*. **2023**, *16*(07), 2340028. https://doi.org/10.1142/S1793604723400283.

73. Mollaamin,F.; S. Shahriari, S.; Monajjemi,M. Monkeypox disease treatment by tecovirimat adsorbed onto single-walled carbon nanotube through drug delivery method, *J. Chil. Chem. Soc.* **2023**, *68*(1), 5796-5801. http://doi.org/10.4067/S0717-97072023000105796.
74. Shahriari, S.; Monajjemi, M.; Mollaamin, F. Determination of proteins specification with SARS- COVID-19 based ligand designing, *J. Chil. Chem. Soc.* **2022**, *67*, 5468-5476. https://doi.org/10.4067/S0717-97072022000205468.
75. Mollaamin, F.; Shahriari, M. Monajjemi, M. Treating omicron BA.4 & BA.5 via herbal antioxidant asafoetida: A DFT study of carbon nanocarrier in drug delivery, *J. Chil. Chem. Soc*. **2023**, *68*(1), 5781-5786. https://doi.org/10.4067/S0717-97072023000105781.
76. Shahriari, S.; Monajjemi, M.; Zare, K. Penetrating to cell membrane bacteria by the efficiency of various antibiotics (clindamycin, metronidazole, azithromycin, sulfamethoxazole, baxdela, ticarcillin, and clavulanic acid) using S-NICS theory, *Biointerface Res. Appl. Chem*. **2018**, *8* (3), 3219 – 3223.
77. Mollaamin, F.; Shahriari, S.; Monajjemi, M. Drug design of medicinal plants as a treatment of omicron variant (COVID-19 variant B.1.1.529), *J. Chil. Chem. Soc*. **2022**, *67*(3), 5562-5570. http://dx.doi.org/10.4067/S0717-97072022000305562.
78. Monajjemi, M.; Mollaamin, F.; Shojaei, S. An overview on coronaviruses family from past to COVID-19: Introduce some inhibitors as antiviruses from Gillan's plants, *Biointerface Res. Appl. Chem.* **2020**, *10*(3), 5575-5585. https://doi.org/10.33263/BRIAC103.575585.
79. Zadeh, M.A.A.; Lari, H.; Kharghanian, L.; Balali, E.; Khadivi, R.; Yahyaei, H.; Mollaamin, F.; Monajjemi, M. Density functional theory study and anti-cancer properties of shyshaq plant: In view point of nano biotechnology, *J. Comput. Theor. Nanosci* **2015**, *12*, 4358–4367, https://doi.org/10.1166/jctn.2015.4366.